Article

TCAD Modelling of Magnetic Hall Effect Sensors

Vartika Pandey, Vlad Marsic [ID], Petar Igic * and Soroush Faramehr *

Centre of E-Mobility and Clean Growth, Coventry University, Coventry CV1 5FB, UK;
pandeyv2@coventry.ac.uk (V.P.); vlad.marsic@coventry.ac.uk (V.M.)
* Correspondence: petar.igic@coventry.ac.uk (P.I.); soroush.faramehr@coventry.ac.uk (S.F.)

Abstract: In this paper, a gallium nitride (GaN) magnetic Hall effect current sensor is simulated in 2D and 3D using the TCAD Sentaurus simulation toolbox. The model takes into account the piezoelectric polarization effect and the Shockley–Read–Hall (SRH) and Fermi–Dirac statistics for all simulations. The galvanic transport model of TCAD Sentaurus is used to model the Lorentz force and magnetic behaviour of the sensor. The current difference, total current, and sensitivity simulations are systematically calibrated against experimental data. The sensor is optimised using varying geometrical and biasing parameters for various ambient temperatures. This unintentionally doped ungated current sensor has enhanced sensitivity to 16.5 %T^{-1} when reducing the spacing between the drains to 1 μm and increasing the source to drain spacing to 76 μm. It is demonstrated that the sensitivity degrades at 448 K (S = 12 %T^{-1}), 373 K (S = 14.1 %T^{-1}) compared to 300 K (S = 16.5 %T^{-1}). The simulation results demonstrate a high sensitivity of GaN sensors at elevated temperatures, outperforming silicon counterparts.

Keywords: gallium nitride; Hall effect; sensors; TCAD

1. Introduction

Over the course of more than a century of development, Hall effect devices have been used to measure magnetic fields, uncover details of carrier transport phenomena in solids, identify the presence of a magnet, and illustrate basic physics principles [1]. Hall effect devices did not become widely used in sensing applications until the development of semiconductor technology. The first commercially accessible Hall effect magnetic sensors were introduced in the mid-1950s, a few years after high-mobility compound semiconductors were discovered. Since then, the development of Hall effect devices has profited from the utilisation of high-quality materials and sophisticated, very efficient production methods made available in the microelectronics industry. However, advancements in microelectronics have also increased the demand for high-quality and reasonably priced sensors. These sensors provide the basis of highly developed and important industrial activity in the modern world [2]. Hall sensors are unique varieties of magnetic sensors that operate according to the Hall effect theory [3]. They are linear devices that are readily integrable [4].

In contrast to typical silicon-based sensors, the gallium nitride sensors can function at high temperatures and have strong magnetic field sensitivity because they possess high electron mobility [5].

The silicon Hall sensors are still in widespread usage today because of their additional benefits of being inexpensive, simple to manufacture, and compatible with complementary metal oxide semiconductor (CMOS) technology. Due to its small bandgap, silicon technology cannot function over 200 °C [6]. Gallium nitride (GaN) technology brings several advantages such as a wider operating temperature range and is energy efficient. It simplifies cooling at the system level, brings a higher current density to applications, and enables a higher breakdown voltage and faster switching frequencies [7] compared to silicon counterparts. It is used in numerous industries including automotive, automation,

and nondestructive testing. Nondestructive testing is a branch of technology that uses magnetic sensors, acoustic sensors, RF-radars, and X-ray scanners to perform tests including radiography, eddy current, ultrasonic, and others.

Nearly all power electronic conversion systems rely heavily on current measurement for device monitoring, efficiency, and reliability increase [8]. To assist the development and deployment of next-generation power electronic systems offering reduced carbon emissions, novel measurement solutions must deliver advanced features including lower loss, higher precision, and a broader working temperature range. This work is focused on the new generation of Hall effect sensors with advanced features based on wide bandgap GaN high electron mobility transistor technology [9]. Since each magnetic sensor technology delivers a certain sensitivity over a finite temperature and frequency range, the gallium nitride (GaN)–based power electronic device derived a new generation of sensors providing a larger bandwidth (1000×), shorter times responses (1/1000), and increased sensitivity (3×) compared to its traditional silicon counterparts. Additionally, it offers a compact design, saving up to 30 cubic centimetres of space when compared with traditional materials, and a wide operating temperature range of −80 °C to 225 °C, suitable for current-measuring solutions while cost effective at the system level [10].

This work highlights a comprehensive study for optimising device performance by combining several elements such as temperature stability and sensitivity of the GaN sensor by varying its geometry and biasing parameters. This all-encompassing approach adds up to the fundamental qualities of GaN-based Hall sensors. The possibility for creating enhanced Hall sensors that can be extensively used in crucial applications involving harsh environments, such as extreme industrial automation and aerospace and automotive systems, is what makes this work significant for the electronics research community. This study also benefits the larger public, providing a viable path for designing cutting-edge sensing technologies that can enhance sustainability, efficiency, and safety across a range of industries by optimising these devices holistically.

This work may deliver a significant contribution for the future integration of GaN power transistor chip technology [11], such as an effective progressive approach in the energy system promising the integration of the sensors for in situ monitoring [12], into the rechargeable batteries used for e-mobility in order to minimise charging times, and to boost battery longevity [13].

In this paper, we present simulation, calibration, analysis and optimisation for Gallium Nitride Magnetic Hall Sensors consist of the following three contacts: a source and a drain divided into two halves—Drain 1 and Drain 2. The current differences between the two drain terminals are computed under different biasing and temperature conditions. Additionally, it is shown that different geometrical variations on the sensor's sensing area can produce significant sensitivity improvements.

2. Materials and Methods

The gallium nitride Hall sensors detect a magnetic flux by using a split drain contact (Figure 1) [14]. These sensors will experience a Lorentz force in the presence of a magnetic field with a strength B that originates from a wire carrying electric current within the circuit [15].

In other words, when a charged particle q is travelling with velocity v in electric field E_y and magnetic field B_z, it experiences a force called the Lorentz force given by the following equation [16]:

$$F = q\left(E_y + v_x \times B_z\right) \tag{1}$$

This is the result of electric and magnetic fields deflecting moving charged carriers within the sensor body, thereby creating a current imbalance measurable between the two drains; this imbalance can then be used to calculate the sensitivity of the sensor through Equation (4) [14].

Sensitivity is mainly split into two types as follows: current-scaled sensitivity and voltage-scaled sensitivity. When the Hall sensor's output voltage varies in direct proportion to the applied magnetic field, it is defined as voltage-scaled sensitivity. This is measured in millivolts per Gauss (mV/G) given by the following equation [6]:

$$S_v = \frac{V_H}{V_s B} \qquad (2)$$

where S_v is the sensitivity with respect to the supply voltage, V_H is the Hall voltage, V_S is the supply voltage, and B is the magnetic field.

When the Hall sensor output's current varies in direct proportion to the applied magnetic field, the value is defined as current-scaled sensitivity. The output is expressed in microamperes per Gauss (µA/G) given by the following equation [6]:

$$S_I = \frac{V_H}{IB} \qquad (3)$$

where S_I is the current-scaled sensitivity, V_H is the Hall voltage, I is the output current, and B is the magnetic field.

When a high degree of accuracy is needed, voltage-scaled sensitivity is desirable, whereas a high degree of precision calls for current-scaled sensitivity [17].
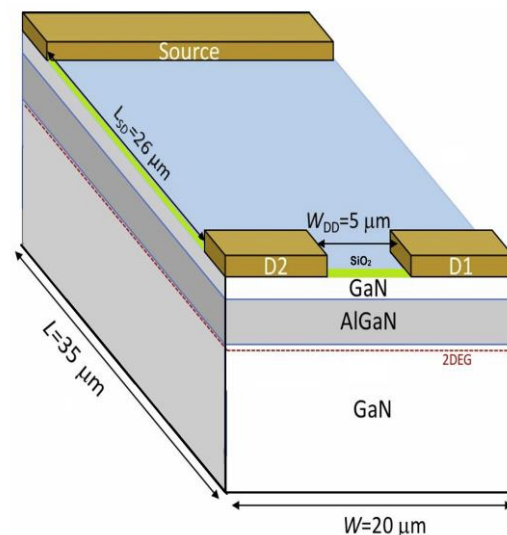

Figure 1. 3D schematic of a simulated gallium nitride Hall sensor [14,18].

2.1. Gallium Nitride Hall Effect Device Structure

Our GaN sensors are developed on a silicon substrate with step-graded AlGaN intermediary layers, resulting in inadvertent doping of $GaN/Al_{0.25}Ga_{0.75}N/GaN$ heterostructures. The thicknesses of the GaN buffer, AlGaN barrier, and GaN cap are 0.002 µm, 0.025 µm, and 1.8 µm, respectively [15]. A four-inch-diameter GaN wafer on a silicon substrate was divided into smaller wafer pieces measuring three centimetres by three centimetres. A specially designed three-mask method was then employed to build various devices onto the tiny wafers. The first mask made it possible to dry etch the wafers and produce mesas, or isolated active zones, using inductively coupled plasma (ICP) [14].

Using physical vapour deposition, the second mask was utilised to create Ohmic contacts by sputter depositing a Ti (20 nm)/Al (100 nm)/Ti (30 nm)/Au (100 nm) metal stack. This was followed by a lift-off procedure and a brief, fast annealing operation at 800 °C in an N_2 environment. Using plasma-enhanced chemical vapour deposition, a conventional SiO_2 passivation layer measuring 100 nm was produced. Lastly, an ICP etch

based on fluorine may be used to remove passivation from the Ohmic contact locations thanks to the third mask [14].

The simulated sensor has a source length of L_S = 4.5 μm and drain length of L_D = 4.5 μm. The source width is 20 μm and both the drain widths are 7.5 μm. The drain to source distance is 26 μm. The overall length and width of the sensor is L = 35 μm and W = 20 μm. The separation between the two drain contacts is W_{DD} = 5 μm. The SiO_2 passivation thickness is t_{SiO2} = 0.02 μm [14]. The sensor is doped with a phosphorus active concentration of 1×10^{17} cm^{-3} and a boron active concentration of 1×10^{15} cm^{-3}. The three contacts are designed and the computational grid is constructed in the simulation program for ensuring the calculation of device parameters. This process delivered the three-dimensional (3D) structural model of the emulated device.

The piezoelectric polarizations are active in all simulations and the electron sheet density is set to N_S = 1×10^{13} cm^{-2} via polarization adjustments. The surface states are placed at $E_C - E_T$ = 2.5 eV with a density of $D_{surface}$ = 4.5×10^{19} cm^{-3}, to define the surface potential. The Shockley–Read–Hall (SRH) and Fermi–Dirac statistics are enabled for all simulations. The mobility model is Caughey–Thomas. Self-heating effects are neglected due to low biasing conditions.

The Lorentz force and magnetic effects are modelled by using the Galvanic transport model of TCAD Sentaurus. The magnetic field (*B*) is applied perpendicular to the surface in units of Tesla (T).

2.2. GaN Hall Sensor Model Setup

Figure 2 is the simulated structure of a 3D GaN Hall effect magnetic sensor in Sentaurus structure editor toolbox. The electric field propagates through the 2-dimensional electron gas (2DEG) until it reaches the source, allowing the electric currents I_{DS1} and I_{DS2} to flow between the source and the drains D1 and D2, respectively, when a positive voltage is provided at D1 and D2. If the drain contacts have the same effective area when there is no magnetic field, then they will be susceptible to current offset because of the alignment error of equal current flow ($I_{DS1} - I_{DS2}$ = 0). Electrons in the currents will be deflected by the applied magnetic field, resulting in current discrepancies, $I_{DS1} - I_{DS2}$ = ΔI. One can calculate the magnetic field value by measuring ΔI [17]. From this measured ΔI value, relative sensitivity of the sensor can be determined by the following equation [14]:

$$S_r = \frac{|I_{DS1} - I_{DS2}|}{I|B|} \times 100\% \tag{4}$$

where S_r is the relative sensitivity measured in Tesla, *I* is the total drain current ($I_{DS1} + I_{DS2}$), and *B* is the applied magnetic field.
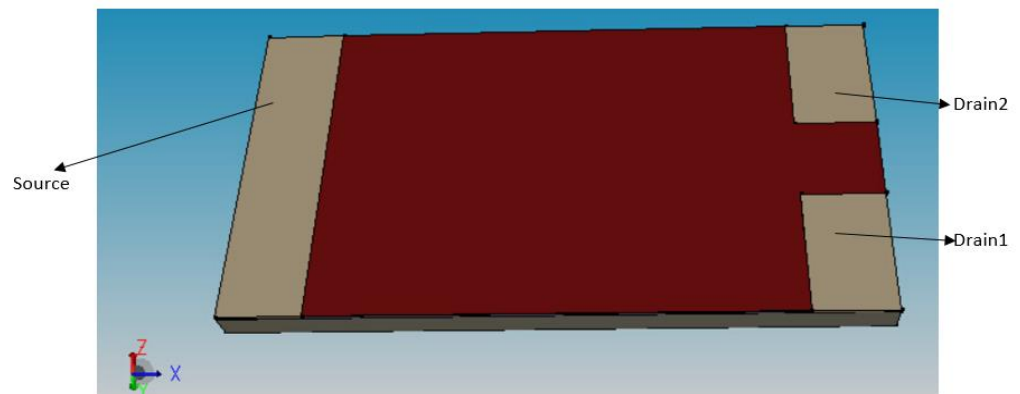

Figure 2. Simulated structure of a 3D GaN Hall effect magnetic sensor visualised using the Sentaurus structure editor toolbox.

In Figure 3a,b, the sensor is optimised for a higher sensitivity for which the optimal ratio of *L/W* is required. The sensitivity depends on *G* (geometric correction factor). The *L/W* ratio varies with *G* and θ_H (Hall angle), given by the following equation [19]:

$$G = 1 - \frac{16}{\pi^2} e^{\frac{-\pi L}{2W}} \left(1 - \frac{8}{9} e^{\frac{-\pi L}{2W}} \right) \left(1 - \frac{\theta_H^2}{3} \right) \tag{5}$$

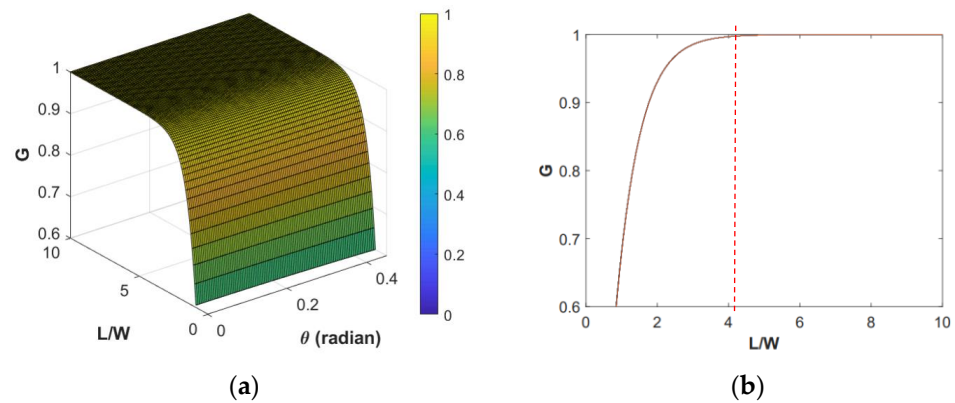where $0 \leq \theta_H \leq 0.45$ radians; and $0.85 \leq \frac{L}{W} \leq$ infinity.

(**a**)   (**b**)

Figure 3. (**a**) *G*, *L/W*, θ_H plotted in 3D; (**b**) *G* vs. *L/W*, where the maximum value of *G* is 1 and the optimal *L/W* ratio is 4.

From Equation (5), *G* depends on the Hall angle and the *L/W* ratio. The Hall angle is the angle of inclination of the current density with respect to the total electric field given by the following equation [1]:

$$\tan \theta_H = \frac{|E_H|}{|E_e|} \tag{6}$$

where $|E_H|$ is the absolute value of the Hall electric field and $|E_e|$ is the external electric field.

The Hall field depends on the current density and the magnetic field given by the relationship [1]:

$$|E_H| = -R_H[J \times B] \tag{7}$$

where R_H is a parameter called the Hall coefficient, *J* is the current density of the sensor surface, and *B* is the magnetic field applied perpendicularly to the sensor in z direction.

The strength and sign of the Hall effect in a given material are described by the Hall coefficient, a material property. The unit of the Hall coefficient is $VmA^{-1}T^{-1}$ (volt metre per ampere Tesla).

The Hall coefficient of strongly extrinsic semiconductors (i.e., the semiconductor material doped with impurities of high concentration to enhance the electrical conductivity and sensitivity of material) is given by the following equation [1]:

$$R_H = -\frac{1}{qn} \tag{8}$$

where *q* is the charge of a single carrier and *n* is the concentration of *n*-type material.

3. Results

3.1. Simulation Results for a 2D GaN Transmission Line Model (TLM)

A transmission line model of GaN in 2D is simulated with the same dimensions as that of the 3D GaN Hall sensor, because the 3D GaN structure is nothing but the drain from the 2D GaN TLM being split into two identically sized halves. The structure of the GaN TLM comprises of a passivation layer SiO_2 along with a GaN cap, a GaN buffer, and an

AlGaN barrier. Nonetheless, the 2D model will only have one drain contact along with a source contact.

A channel is formed on the interface of the GaN buffer and the AlGaN barrier. Figure 4 shows the energy band diagram and electron density. E_C is the conduction band energy, which refers to the energy at the bottom of the conduction band in the semiconductor, while E_T is the trap energy level, which refers to the energy of a trap state within the band of the semiconductor. The surface states are placed at $E_C - E_T = 0.67$ eV with a density of $D_{surface} = 4.5 \times 10^{19}$ cm^{-3} to define the surface potential. The capture cross section of the electrons and holes are set to 1×10^{-14} cm^2 [20].
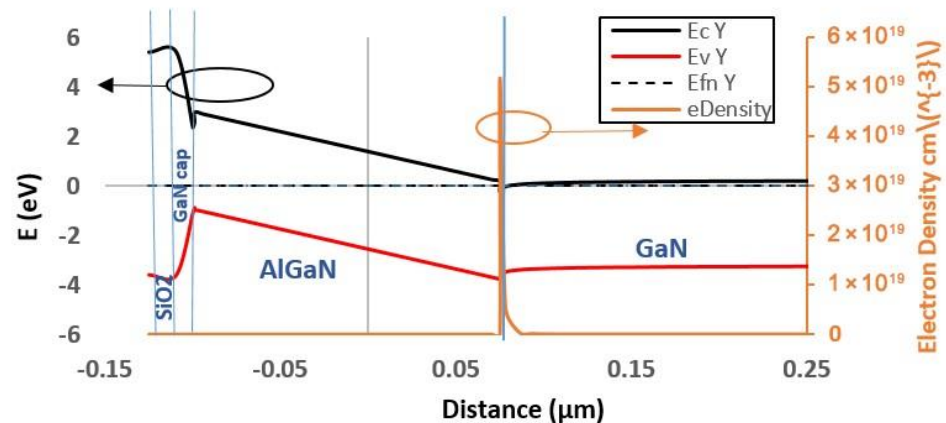

Figure 4. Simulated energy band diagram (black and red line plot) and electron density (brown line plot) for 2D GaN TLM at an equilibrium of 300 K.

The electron density is shown on the right axis, and energy is defined on the left. The black line shows the conduction energy band, the red line shows the valance energy band, while the black dotted line depicts the Fermi level. The 2-dimensional electron gas layer formed at the interface of the GaN buffer and AlGaN barrier is shown by an orange peak in the middle.

As shown in Figure 5, as the applied drain voltage gradually increases from 0 V to 1 V, the drain current also surges. This is recorded at a room temperature of 300 K. With a surge in the drain voltage, the flow of electrons in the 2 DEG channel will be more, hence the rise in drain current.
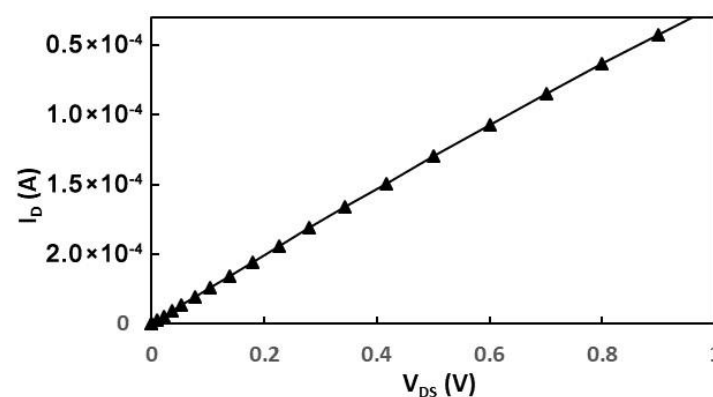

Figure 5. Simulated drain current (A) against drain to source voltage (V) sweeping from 0 V to 1 V of TLM at 300 K.

3.2. Simulation Results for a Gallium Nitride Hall Sensor

The GaN Hall sensor contains a GaN buffer layer, an AlGaN barrier, and a GaN cap along with a passivation layer. From Figure 6b, a coarser mesh is applied to the GaN buffer because it is a large uniform area, while a finer mesh is considered for the interface

between the GaN and AlGaN and on the GaN cap to reduce the computational time and improve accuracy.
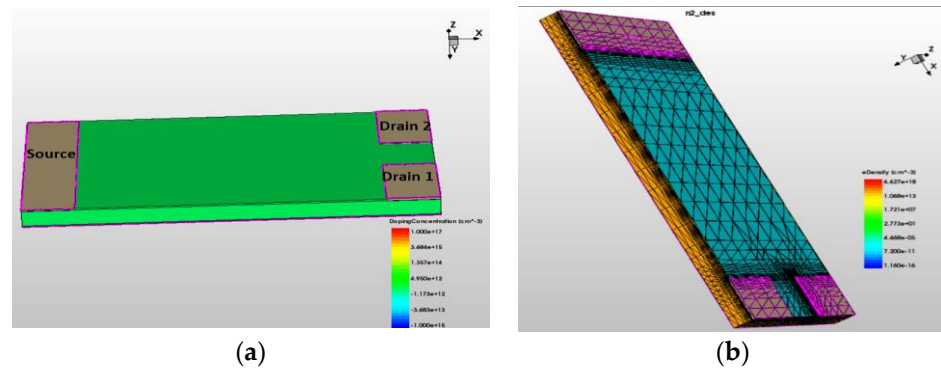

Figure 6. (**a**) Simulated GaN Hall sensor in 3D with contacts as source, Drain 1, and Drain 2 at equilibrium (i.e., 0 V biasing of source under 300 K); (**b**) GaN Hall sensor at the surface mesh.

In Figure 7a, when a sweeping voltage of 0 to 1 V is applied across the drains, the total current from both drains is obtained at different temperatures. It is observed that the total current falls with each temperature rise. This is mainly due to the degradation in mobility due to the increase in scattering mechanisms within the sensor [14,21–23].
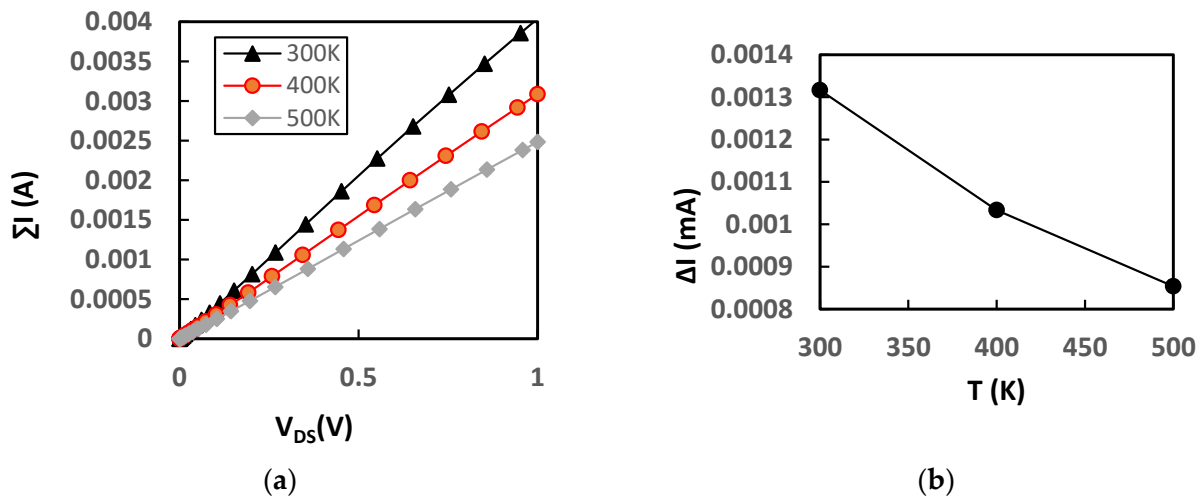

Figure 7. (**a**) Simulated total current (A) from Drain 1 and Drain 2 vs. drain source voltage (V) at different temperatures of 300 K, 400 K, and 500 K at voltage sweeping from 0 to 1 V. (**b**) Simulated current imbalance (mA) vs. temperature (K) when the sensor is applied to a drain voltage of 1 V against an increasing magnetic field strength (B = 0 to 30 mT) at 300 K, 400 K, and 500 K.

The current imbalance measured between D1 and D2 contacts rises when increasing the magnetic field's strength as shown in Figure 7b, although the total current and the estimated imbalance decrease as temperature increases.

3.3. Validation

The 3D GaN simulations are validated in Figures 8 and 9 where the sensor is simulated for current imbalance against the magnetic field sweeping from 0 to 30 mT, and the sensor output current against the drain source voltage sweeping from 0 to 0.5 V. For the simulation and experiment results, both are verified at elevated temperatures of 300 K, 373 K, and 448 K.
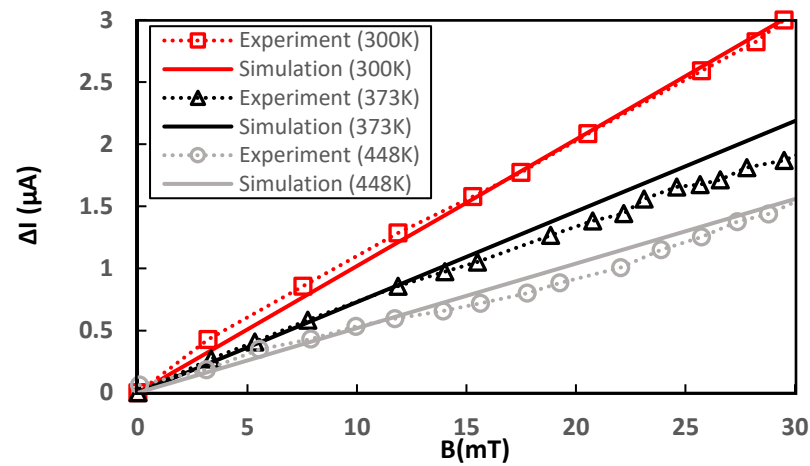
Figure 8. Simulated current imbalance (μA) from Drain 1 and Drain 2 against drain source voltage varying from 0 to 0.5 V at elevated temperatures of 300 K, 373 K, and 448 K.
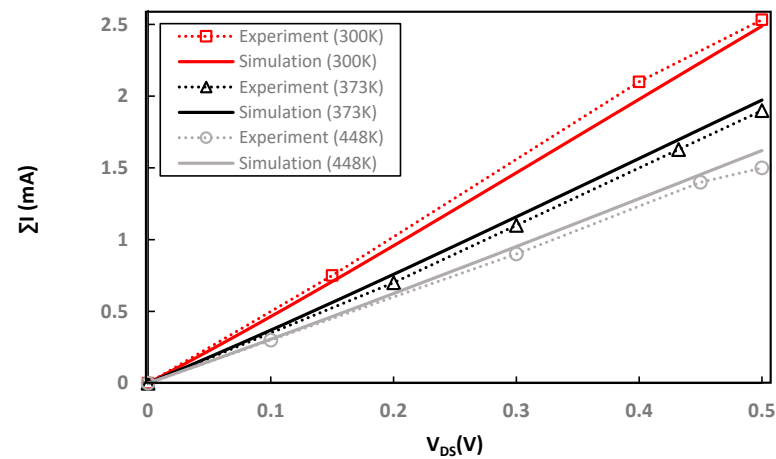

Figure 9. Simulated total current (mA) from Drain 1 and Drain 2 against magnetic field sweeping from 0 to 30 mT at 300 K, 373 K, and 448 K at an applied voltage sweeping from 0 to 0.5 V.

Figure 10a shows the sensitivity of the GaN sensor as the temperature rises from 300 K to 448 K, while Figure 10b illustrates the sensitivity of the sensor against increasing the magnetic field from 0 to 30 mT for both the experiment and the simulation, where the dotted line is the experiment graph and the straight line is from the simulation. The sensitivity falls as expected with increasing temperature.
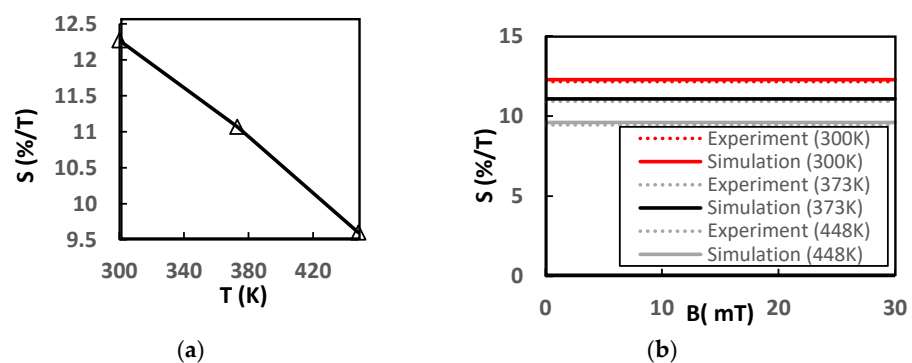

(a)

(b)

Figure 10. (**a**) Sensor sensitivity (%T^{-1}) against temperature (K). (**b**) Sensor sensitivity (%T^{-1}) against magnetic field sweeping from 0 to 30 mT at 300 K, 373 K, and 448 K from the simulation and the experiment.

The sensitivity remains constant with the increasing magnetic field, with the experimental data from the TCAD simulation showing a good agreement with the previous work's experimental data [24]. The Hall sensor's sensitivity should not be misinterpreted for the sensor's current or voltage differential output measurement, which linearly varies with the magnetic field density until reaching the saturation zones for the north pole and, symmetrically, for the south pole, such as presented in [11].

3.4. Optimisation

Figures 11–13 represent the current difference, total current, and sensitivity at V_{DS} = 0.5 V when the electron mobility is 1700 $cm^2V^{-1}-s$ with the sensor's dimensions as L = 80 μm, W = 20 μm, W_{DD} = 5 μm, 2 μm, 1 μm, and L_{SD} = 71 μm. The current difference, total current, and sensitivity degrades with increasing the distance between the split drains. As the drains are away from each other, the drain resistance is less, which increases the total current flowing in the device, causing the current deflection to decrease, resulting in a lower Lorentz force. Hence, degrading the sensitivity [25].
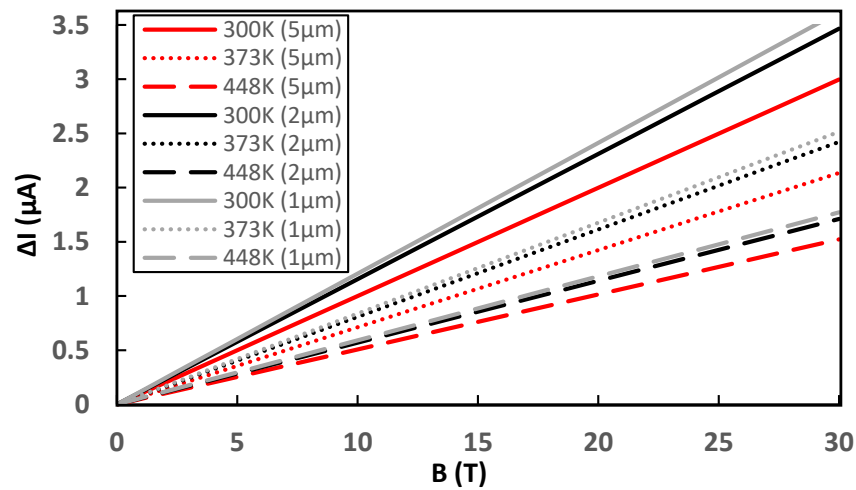

Figure 11. Simulated total current (μA) from Drain 1 and Drain 2 against magnetic field sweeping from 0 to 30 mT at 300 K, 373 K, and 448 K at an applied voltage sweeping from 0 to 0.5 V. The sensor's dimensions are L = 80 μm, W = 20 μm, W_{DD} = 5 μm, 2 μm, 1 μm, and L_{SD} = 71 μm.
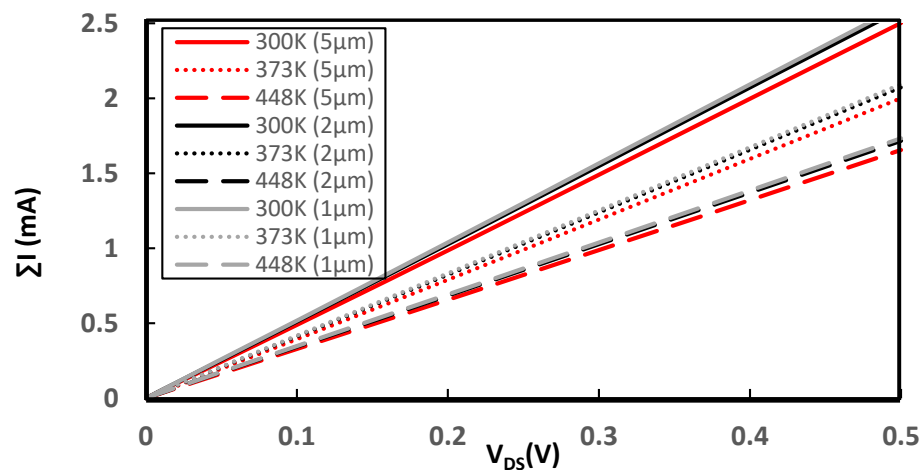

Figure 12. Simulated current imbalance (mA) from Drain 1 and Drain 2 against drain source voltage varying from 0 to 0.5 V at elevated temperatures of 300 K, 373 K, and 448 K. The sensor's dimensions are L = 80 μm, W = 20 μm, W_{DD} = 5 μm, 2 μm, 1 μm, and L_{SD} = 71 μm.
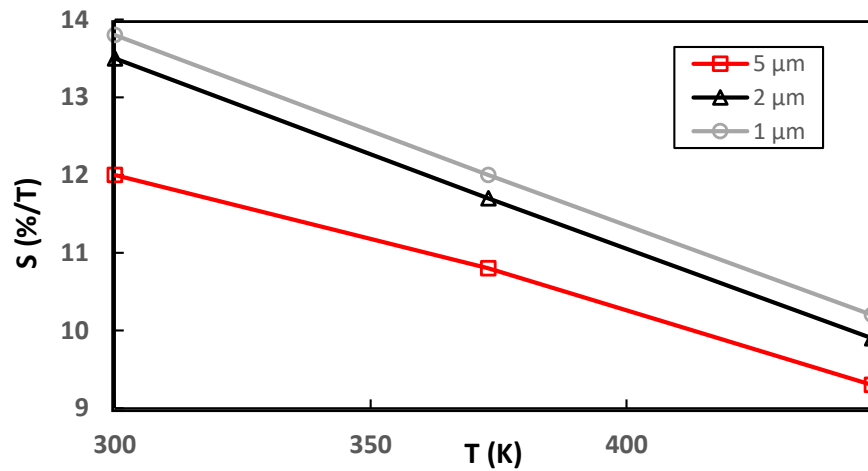
Figure 13. The sensor's sensitivity ($\%T^{-1}$) against temperatures of 300 K, 373 K, and 448 K. The sensor's dimensions are L = 80 µm, W = 20 µm, W_{DD} = 5 µm, 2 µm, 1 µm, and L_{SD} = 71 µm.

Figures 14–16 represent the current difference, total current, and sensitivity at V_{DS} = 0.5 V when the electron mobility is 1700 cm^2 V^{-1} − s with the sensor's dimensions as L = 80 µm, W = 20 µm, W_{DD} = 5 µm, 2 µm, 1 µm, and L_{SD} = 76 µm. The current difference, total current, and sensitivity improves as the distance between the source and drain is increased. When the source contact width is scaled down, the effective contact area reduces, causing the total current flowing in the device to decrease. The current deflection increases resulting in a larger Lorentz force and improving the sensitivity. Also, from Equation (6), when current density reduces, it diminishes the Hall electric field, which causes the Hall angle to drop-off because the Hall angle is proportional to the Hall electric field. When the Hall angle reduces, the geometric correction factor increases and the sensor's sensitivity also improves [25].
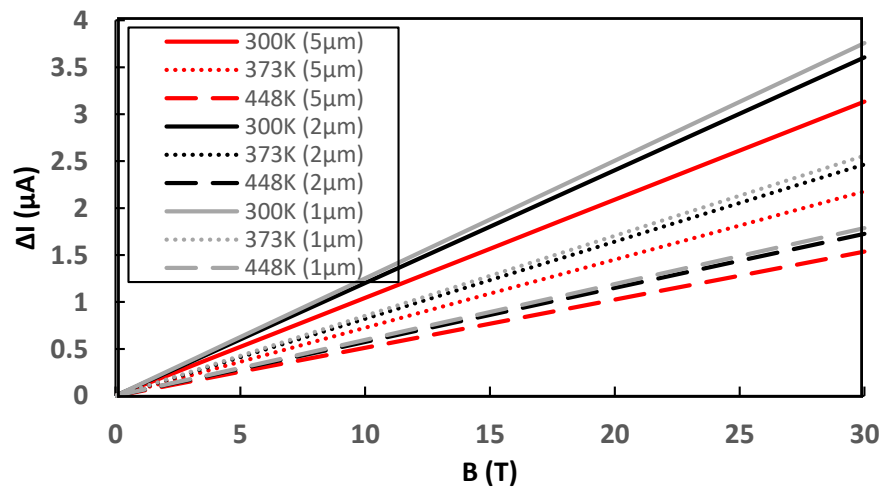

Figure 14. Simulated total current (µA) from Drain 1 and Drain 2 against magnetic field sweeping from 0 to 30 mT at 300 K, 373 K, and 448 K at applied voltage sweeping from 0 to 0.5 V. The sensor's dimensions are L = 80 µm, W = 20 µm, W_{DD} = 5 µm, 2 µm, 1 µm, and L_{SD} = 76 µm.
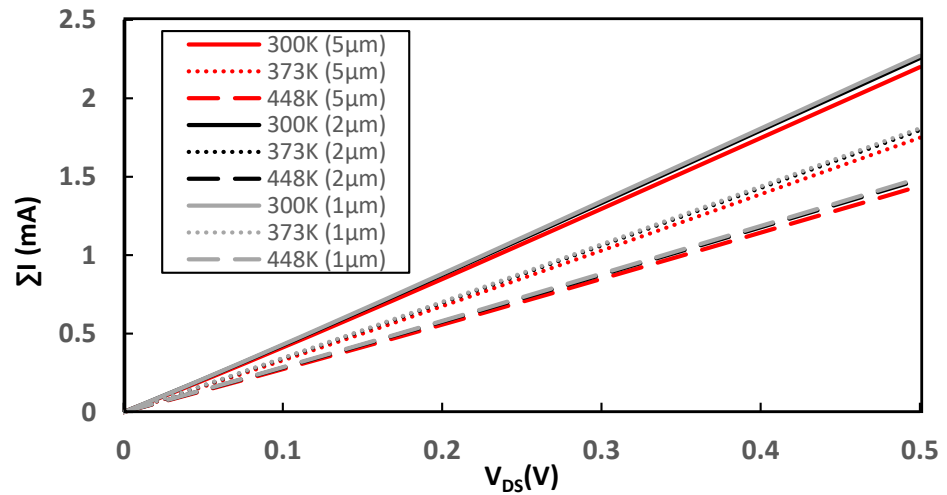
Figure 15. Simulated current imbalance (mA) from Drain 1 and Drain 2 against drain source voltage varying from 0 to 0.5 V at elevated temperatures 300 K, 373 K, and 448 K. The sensor's dimensions are L = 80 μm, W = 20 μm, W_{DD} = 5 μm, 2 μm, 1 μm, and L_{SD} = 76 μm.

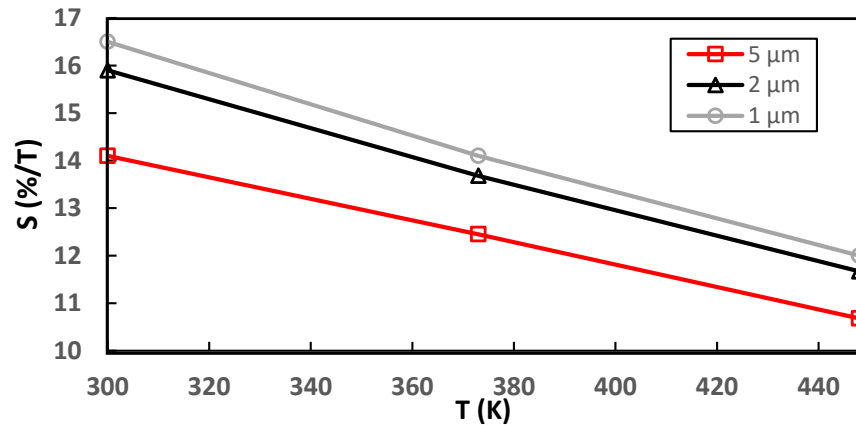**Figure 16.** The sensor's sensitivity (%T^{-1}) against temperatures of 300 K, 373 K, and 448 K. The sensor's dimensions are L = 80 μm, W = 20 μm, W_{DD} = 5 μm, 2 μm, 1 μm, and L_{SD} = 76 μm.

4. Discussion

The GaN sensor is simulated and presented by Figure 6a. The drains are of equal length and width so as to avoid unwanted offsets when there is no magnetic field. Highly doped regions are created by the drain contacts, which are Ohmic in nature to repose the fields and thermionic emissions [25]. Figure 6b illustrates the meshing profile of the modelled sensor's surface plane. It is very complex to mesh the model in three dimensions because the coarser the mesh, the larger the convergence issues, leading to faults in current deflection in absence of the magnetic field. A small mesh involves more elements on the same surface than a coarse one; therefore, despite the accuracy increasing, the simulation speed decreases while more computational resources are required (i.e., CPU power, RAM, parallel computing capabilities, etc.). That is why, when there is large homogenous area (without details), coarse mesh is used and the finer mesh is only used for the details. Here in the 3D GaN model, a coarser mesh is applied to the GaN buffer because it is a large uniform area, while a finer mesh is considered for the interface of GaN and AlGaN, and on the GaN cap to improve the speed and accuracy of the simulation results.

In Figure 3a,b, to obtain the ideal value for the *L/W* ratio, Matlab is used to visualise Equation (5). Since sensitivity is dependent on the *L/W* ratio, finding the ideal value is necessary for sensor optimisation. Regarding the 3D plot for G, L/W, and θ_H, where G is the geometrical correction factor varying from 0 to 1 and θ_H ranges from 0 to 0.45 radians,

plotting G against *L/W* shows that *L/W* begins to increase and becomes a constant line when *L/W* approaches 4. Thus, the graphic illustrates that 4 is the ideal *L/W* ratio.

A transmission line model (TLM) of GaN in 2D is simulated before the 3D model, keeping the dimensions the same as that of the 3D GaN Hall sensor. A channel is formed on the interface of the GaN buffer and the AlGaN barrier. Figure 4 shows the energy band diagram and electron density of this 2D GaN TLM model. E_C is the conduction band energy, which refers to the energy at the bottom of the conduction band in the semiconductor, while E_T is the trap energy level, which refers to the energy of a trap state within the band of the semiconductor. The surface states are placed at $E_C - E_T = 0.67$ eV with a density of $D_{surface} = 4.5 \times 10^{19}$ cm^{-3} to define the surface potential. The capture cross section of electrons and holes are set to 1×10^{-14} cm^2. The GaN sensor is composed of a passivation layer of SiO_2, a GaN cap, an AlGaN barrier, and a GaN buffer. In the GaN cap region, the conduction band E_c and valance band E_v show band bending due to the presence of the electric field. In the AlGaN layer, a significant bending is observed due to the polarization effects and formation of a two-dimensional electron gas layer at the interface of the AlGaN barrier and the GaN buffer. Then, the bands in the GaN buffer region become flat, indicating the equilibrium conditions with no significant band bending. The band bending of E_c and E_v is important for the confinement of electrons in 2DEG. In the AlGaN/GaN region, a high electron concentration is indicated by the Fermi level located above the conduction band edge. The electron density is illustrated on the right axis with orange circular marking and energy is defined on the left with black circular marking.

Figure 5 simulates the drain current against the drain voltage of the GaN TLM at a voltage sweeping from 0 to 1 V. The drain current grows in tandem with the drain voltage as the voltage progressively climbs from 0 to 1 V. The higher the drain voltage, the stronger the Lorentz force and the electric field, increasing the flow of electrons in the 2 DEG channel.

Figure 7a presents the simulated total current from Drain 1 and Drain 2 against drain source voltage at different temperatures of 300 K, 400 K, and 500 K at an applied voltage sweeping from 0 to 1 V. This suggests that when the temperature rises, the combined current from both drains decreases. The primary cause of this is the reduction in mobility brought on by the sensor's increased number of scattering mechanisms. Figure 7b mimics current imbalance vs. temperature. At 300 K, 400 K, and 500 K, the drain voltage is 1 V as opposed to a rising magnetic field intensity ($B = 0$ to 30 mT). As the intensity of the magnetic field increases, so does the current imbalance measured between the two drain contacts. However, when the temperature rises, both the total current and the current imbalance drop.

The 3D GaN simulations are validated in Figures 8 and 9 where the sensor is simulated for current imbalance against magnetic field sweeping from 0 to 30 mT, and sensor output current against drain source voltage sweeping from 0 to 0.5 V. For simulation and experiment, both are verified at temperatures of 300 K, 373 K, and 448 K. As previously mentioned, an increase in the magnetic field and drain source voltage will cause the current imbalance and total current to rise; however, an increase in temperature will cause both to drop because of a decrease in mobility and saturation velocity. GaN sensors are subject to a variety of scattering phenomena, including phonon scattering [26], dislocation scatterings [27], ionized impurity scatterings [28], and interface roughness between the AlGaN top layer and the 2DEG channel. Mobility has been demonstrated to be impacted by ionized impurity scattering at low temperatures, but when temperatures rise over 300 K, phonon scattering takes over as the primary source of scattering [23,26,29]. Furthermore, both high and low temperatures may be influenced by surface roughness [26]. Since all of the temperatures examined in this work were higher than 300 K, surface roughness and phonon scattering are thought to have had a role in the decreasing current that was seen [26,30].

When the temperature rises from 300 K to 448 K, the sensitivity decreases from 12.27% to 9.6%, as illustrated in Figure 10a,b. The drop in relative sensitivity found at increasing

temperatures is attributed to the mobility deterioration of electrons in the 2DEG channel due to increased phonon scattering [26].

The sensor is tuned to increase sensitivity. The geometric correction factor has a direct correlation with sensitivity. The formula of G, provided by Equation (5), indicates that it relies on the Hall angle and L/W ratio. The L/W ratio is optimal at 4, as seen in Figure 3b. The length and width are scaled up by ratio 4 for the next set of simulations, so that L = 80 μm and W = 20 μm. To achieve optimisation, two parameters are changed as follows: in the first scenario, as illustrated by Figures 11–13, which show the simulations for current imbalance, total current, and sensitivity, the distance between drain 1 and 2 is shortened while maintaining the drain and source distance at 71 μm.

In the second scenario, the scaled-up distance (76 μm) between the drain and source (71 μm) is displayed in Figures 14–16 for current imbalance, total current, and sensitivity. At ambient temperature, the sensitivity decreases from 13.8% to 12% when W_{DD} increases from 1 μm to 5 μm and L_{SD} = 71 μm. At higher temperatures, however, sensitivity considerably reduces. When drains are spaced apart, the drain resistance decreases, increasing the total current flowing through the device and reducing the current deflection, which lowers the Lorentz force, degrading the sensitivity as a result.

In the second case, the sensitivity improves to 16.5% from 13.8% at constant W_{DD} of 1 μm when L_{SD} increases from 71 μm to 76 μm at a room temperature of 300 K. The total current, current difference, and the sensitivity improves as the distance between the source and the drain is increased. The effective contact area shrinks with a drop in source contact width, which also results in a decrease in the device's overall current flow. As the current deflection rises, a significant Lorentz force is produced, increasing sensitivity. Additionally, given that the Hall angle is proportionate to the Hall electric field, Equation (6) shows that a decrease in current density also results in a decrease in the Hall electric field. Both the sensitivity and the geometric correction factor rise with a decrease in the Hall angle. Table 1 illustrates the sensitivity ($\%\mathrm{T}^{-1}$) of the gallium nitride Hall sensor being optimised for both the cases.

Table 1. Sensitivity ($\%\mathrm{T}^{-1}$) optimized for the gallium nitride Hall sensor.

Temperature (K)	L_{SD} = 71 μm	L_{SD} = 76 μm	L_{SD} = 71 μm	L_{SD} = 76 μm	L_{SD} = 71 μm	L_{SD} = 76 μm
	W_{DD} = 5 μm		W_{DD} = 2 μm		W_{DD} = 1 μm	
300 K	12%	14.1%	13.5%	15.9%	13.8%	16.5%
373 K	10.8%	12.45%	11.7%	13.68%	12%	14.1%
448 K	9.3%	10.68%	9.9%	11.67%	10.2%	12%

5. Conclusions

The findings of this paper demonstrate the capabilities of the new generation split drains GaN Hall sensor simulated in TCAD software. Current difference, total current, and sensitivity simulations of the GaN Hall sensor are illustrated in this paper. These results are then calibrated against the measurements for validation purpose. The sensor shows a decrease in sensitivity at elevated temperatures as demonstrated. The sensor is optimised and it shows that scaling up the source to drain spacing and reducing the split drains increases the relative sensitivity of GaN Hall sensors. Reducing the spacing between the drains to 1 μm and increasing the source to drain spacing to 76 μm optimises the sensor's sensitivity to 16.5 $\%\mathrm{T}^{-1}$. The sensor was simulated at an elevated temperature of 448 K, demonstrating its ability to function even in challenging environments.

Author Contributions: Conceptualization, V.P. and S.F.; methodology, V.P. and S.F.; formal analysis, V.P. and S.F.; investigation, V.P.; writing—original draft preparation, V.P.; writing—review and editing, V.P., V.M., S.F. and P.I.; supervision, S.F. and P.I. All authors have read and agreed to the published version of the manuscript.

Data Availability Statement: The raw data supporting the conclusions of this article will be made available by the authors on request.

Conflicts of Interest: The authors declare no conflicts of interest.

References

1. Dance, B. Hall Effect Devices. *New Electron.* **1982**, *15*, 82–84. [CrossRef]
2. Rigelsford, J. Magnetic Sensors and Magnetometers. *Sens. Rev.* **2002**, *22*, 645. [CrossRef]
3. Xu, H.; Zhang, Z.; Shi, R.; Liu, H.; Wang, Z.; Wang, S.; Peng, L.M. Batch-fabricated high-performance graphene Hall elements. *Sci. Rep.* **2013**, *3*, 1207. [CrossRef] [PubMed]
4. Crescentini, M.; Syeda, S.F.; Gibiino, G.P. Hall-Effect Current Sensors: Principles of Operation and Implementation Techniques. *IEEE Sens. J.* **2022**, *22*, 10137–10151. [CrossRef]
5. Fan, L.; Bi, J.; Xi, K.; Majumdar, S.; Li, B. Performance optimization of FD-SOI hall sensors via 3D TCAD simulations. *Sensors* **2020**, *20*, 2751. [CrossRef] [PubMed]
6. Alpert, H.S.; Dowling, K.M.; Chapin, C.A.; Yalamarthy, A.S.; Benbrook, S.R.; Köck, H.; Ausserlechner, U.; Senesky, D.G. Effect of Geometry on Sensitivity and Offset of AlGaN/GaN and InAlN/GaN Hall-Effect. *IEEE Sens. J.* **2019**, *19*, 3640–3646. [CrossRef]
7. Letellier, A.; Dubois, M.R.; Trovao, J.P.; Maher, H. Gallium Nitride Semiconductors in Power Electronics for Electric Vehicles: Advantages and Challenges. In Proceedings of the 2015 IEEE Vehicle Power and Propulsion Conference (VPPC), Montreal, QC, Canada, 19–22 October 2015; pp. 1–6. [CrossRef]
8. Von Kluge, J.W.A.; Langheinrich, W.A. An analytical model of MAGFET sensitivity including secondary effects using a continuous description of the geometric correction factor G. *IEEE Trans. Electron Devices* **1999**, *46*, 89–95. [CrossRef]
9. Marsic, V.; Faramehr, S.; Igic, P. Coil Design for Integration with GaN Hall-Effect Sensors. In Proceedings of the 2022 IEEE Workshop on Wide Bandgap Power Devices and Applications in Europe (WiPDA Europe), Coventry, UK, 18–20 September 2022; pp. 1–5. [CrossRef]
10. Popović, R.S. Hall-effect devices. *Sens. Actuators* **1989**, *17*, 39–53. [CrossRef]
11. Marsic, V.; Faramehr, S.; Fleming, J.; Bhagat, R.; Igic, P. GaN Transistors' Radiated Switching Noise Source Evidenced by Hall Sensor Experiments Toward Integration. *IEEE Access* **2024**, *12*, 13783–13794. [CrossRef]
12. Fleming, J.; Amietszajew, T.; Roberts, A. In-situ electronics and communications for intelligent energy storage. *HardwareX* **2022**, *11*, e00294. [CrossRef]
13. Amietszajew, T.; McTurk, E.; Fleming, J.; Bhagat, R. Understanding the limits of rapid charging using instrumented commercial 18650 high-energy Li-ion cells. *Electrochim. Acta* **2018**, *263*, 346–352. [CrossRef]
14. Thomas, B.R.; Faramehr, S.; Moody, D.C.; Evans, J.E.; Elwin, M.P.; Igic, P. Study of GaN dual-drain magnetic sensor performance at elevated temperatures. *IEEE Trans. Electron Devices* **2019**, *66*, 1937–1941. [CrossRef]
15. Rodríguez-Torres, R.; Gutiérrez-Domínguez, E.A.; Klima, R.; Selberherr, S. Analysis of split-drain MAGFETs. *IEEE Trans. Electron Devices* **2004**, *51*, 2237–2245. [CrossRef]
16. Michaud, A. Demystifying the Lorentz Force Equation. *J. Mod. Phys.* **2022**, *13*, 776–838. [CrossRef]
17. Igic, P.; Jankovic, N.; Evans, J.; Elwin, M.; Batcup, S.; Faramehr, S. Dual-Drain GaN Magnetic Sensor Compatible with GaN RF Power Technology. *IEEE Electron Device Lett.* **2018**, *39*, 746–748. [CrossRef]
18. Faramehr, S.; Poluri, N.; Igic, P.; Jankovic, N.; De Souza, M.M. Development of GaN Transducer and On-Chip Concentrator for Galvanic Current Sensing. *IEEE Trans. Electron Devices* **2019**, *66*, 4367–4372. [CrossRef]
19. Paun, M.A.; Sallèse, J.M.; Kayal, M. Geometry influence on the Hall effect devices performance. *UPB Sci. Bull. Ser. A Appl. Math. Phys.* **2010**, *72*, 257–271.
20. Faramehr, S.; Kalna, K.; Igic, P. Modeling of 2DEG and 2DHG in i-GaN capped AlGaN/AlN/GaN HEMTs. In Proceedings of the 2014 29th International Conference on Microelectronics Proceedings—MIEL 2014, Belgrade, Serbia, 12–14 May 2014; pp. 81–84. [CrossRef]
21. Zhang, Z.; Zhang, J.; Xu, Z.; Duan, H.; Hao, Y. High temperature electron transport properties of AlGaN/GaN heterostructures with different Al-contents. *Sci. China Ser. G Phys. Mech. Astron.* **2009**, *52*, 1879–1884. [CrossRef]
22. Aktas, O.; Fan, Z.F.; Mohammad, S.N.; Botchkarev, A.E.; Morkoç, H. High temperature characteristics of AlGaN/GaN modulation doped field-effect transistors. *Appl. Phys. Lett.* **1996**, *69*, 3872–3874. [CrossRef]
23. Pramanick, M.S.; Ghosal, A. Effects of scattering on transport properties in GaN. In Proceedings of the 2017 Devices for Integrated Circuit (DevIC), Kalyani, India, 23–24 March 2017; pp. 647–651. [CrossRef]
24. Marsic, V.; Faramehr, S.; Fleming, J.; Bhagat, R.; Igic, P. Understanding the limits of a Hall sensor sensitivity for integration on a GaN power transistor chip: Experiments with market available components. In Proceedings of the 12th International Conference on Power Electronics, Machines and Drives (PEMD 2023), Brussels, Belgium, 23–24 October 2023; pp. 350–356. [CrossRef]

25. Faramehr, S.; Janković, N.; Igić, P. Analysis of GaN MagHEMTs. *Semicond. Sci. Technol.* **2018**, *33*, 095015. [CrossRef]
26. Pichonat, E.; Kuzmik, J.; Bychikhin, S.; Pogany, D.; Poisson, M.A.; Grimbert, B.; Gaquière, C. Temperature analysis of AlGaN/GaN high-electron-mobility transistors using micro-Raman scattering spectroscopy and transient interferometric mapping. In Proceedings of the 2006 European Microwave Integrated Circuits Conference, Manchester, UK, 10–13 September 2006; pp. 54–57. [CrossRef]
27. Karthik, R.; Sathyakam, P.U.; Mallick, P.S. Effect of dislocation scattering on electron mobility in GaN. *Nat. Sci.* **2011**, *3*, 812–815. [CrossRef]
28. Schubert, F.; Wirth, S.; Zimmermann, F.; Heitmann, J.; Mikolajick, T.; Schmult, S. Growth condition dependence of unintentional oxygen incorporation in epitaxial GaN. *Sci. Technol. Adv. Mater.* **2016**, *17*, 239–243. [CrossRef] [PubMed]
29. Gurusinghe, M.N.; Davidsson, S.K.; Andersson, T.G. Two-dimensional electron mobility limitation mechanisms in $Al_xGa_{1-x}N$/GaN heterostructures. *Phys. Rev. B* **2005**, *72*, 045316. [CrossRef]
30. Asgari, A.; Babanejad, S.; Faraone, L. Electron mobility, Hall scattering factor, and sheet conductivity in AlGaN/AlN/GaN heterostructures. *J. Appl. Phys.* **2011**, *110*, 113713. [CrossRef]